Article

Electromagnetic Characterization of Permanent Magnet Eddy Current Structures Based on Backplane Distance Adjustment

Yipeng Wu [1] , **Teng Wang** [1,2,3,4,*], **Tao Song** [1,2,3,4] **and Wenxiao Guo** [1,2,3,4]

1　China Coal Research Institute, Beijing 100013, China; wu1997@alumni.tongji.edu.cn (Y.W.);
　　bingzi0127@sina.com (T.S.); gwx041202@163.com (W.G.)
2　CCTEG Taiyuan Research Institute Co., Ltd., Taiyuan 030006, China
3　Shanxi Tiandi Coal Mining Machinery Co., Ltd., Taiyuan 030006, China
4　China National Engineering Laboratory for Coal Mining Machinery, Taiyuan 030006, China
*　Correspondence: wangteng40@126.com

Abstract: To address the problem of problematic spray design inside mining anchor-digging equipment, a switching seal using a permanent magnet eddy current drive is initially presented here. The layer model of the permanent magnet eddy current structure is established, the subdomain analysis model is introduced, the permanent magnet eddy current structure is divided into six regions along the axial direction, and the boundary equations are established at the interfaces of each region. The vector magnetic potential equations in each region are deduced, along with the electromagnetic torque and axial force equations. The computational results are compared and analyzed with the results of finite element simulation, verifying the accuracy of the theoretical model. The design of experiments is used to verify the feasibility of the switching seal using the permanent magnet eddy current structure.

Keywords: switch seal; permanent magnet drive; electromagnetic field design; split-variable method

1. Introduction

The internal spraying system of mining anchor-digging equipment is a technical device used for adsorbing and settling dust on the underground mining face, reducing the temperature of the cutting teeth, and eliminating sparks, with the effect of improving the visibility of the working face, improving the working environment, and increasing the service life of the equipment. Because of its need to cut coal rock, its working speed is generally around 20–50 rpm. It has a rotating water seal diameter, problems with short service life, and the transverse axis of the retractable drum-digging anchor-integrated machine is due to the structural design of the outer rotor, where the retractable cylinder needs to provide a hydraulic oil pipeline. This special mechanical structure design causes difficulties with the outer rotor drum as well as the internal runners into the water [1]. The structure of the transverse telescopic cut-off drum and the internal piping is shown in Figure 1. Inside the speed reducer, there are two hydraulic channels: the extension channel (13) and the retraction channel (14), which make it impossible for the internal spray system, which is located under the cut-off drum teeth, to feed water from the outer drum.

Failure or non-functioning of the internal spray system may not only lead to premature failure of the cutting pick, affecting the mining progress of the working face, but also lead to major safety accidents caused by sparking of the cutting pick. For this reason, the authors have designed a switching mechanical seal using permanent magnetic eddy current transmission under the premise of replacing the telescopic cylinder with a water-medium cylinder, where under the shutdown condition the pressurized water will be directed to the water-medium telescopic cylinder, which can carry out telescopic action to direct the pressurized water to the internal spraying nozzle on the drum during the rotation of the cut-off drum. This structure is characterized by changing the compensation element of

the traditional mechanical seal [2] from a spring to a permanent magnet drive structure. In order to regulate the axial force of the permanent magnet eddy current structure, a backplane is set behind the copper disc, and the distance between the backplane and the copper disc needs to be designed according to the sealing requirements. Due to this disc-type permanent magnet structure of the conductor disc assembly, there is no concise, ready-made formula available for the axial force on the magnet disc assembly, while the design of the axial force is the key to the success or failure of this mechanical seal.
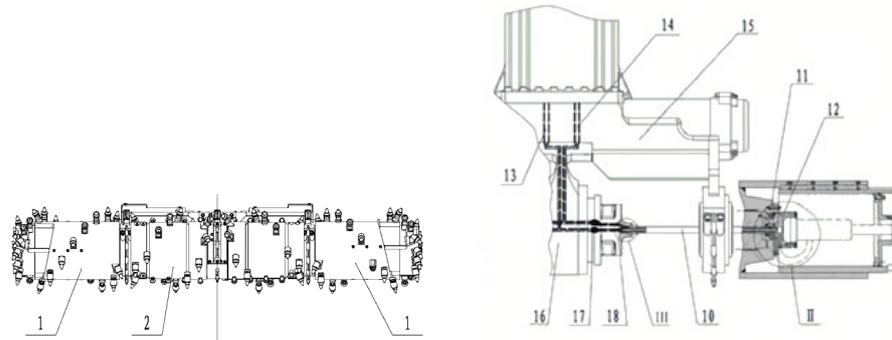
Figure 1. Dual-drive telescopic drum cut-off mechanism for integrated anchor-digging machines and the oil channel in the reducer of the drum. The dotted line shows the installation position of the telescopic hydraulic cylinder with the structure of the telescopic cutting drum.

Existing studies at home and abroad mainly focus on solid disc PM coupler [3] and disc PM coupler [4] structures with slotted conductor discs, where the conductor disc backplanes of these PM eddy current structures are tightly attached to the conductor discs. The electromagnetic field modeling and analysis methods for this type of PM coupler usually include analytical and numerical methods. The commonly used analytical methods for solving the electromagnetic field include the equivalent magnetic circuit method [5], the equivalent magnetic charge method [6], the equivalent current method [7], the separated variables method [8], and the conformal transformation method [9]. Although the equivalent magnetic circuit method can solve complex models, the results tend to have large errors due to its oversimplification of the complex model in the calculations [5]. A.C. Smith [10] used the layer model approach to model the magnetic field of a permanent magnet coupler with axial flux and used the separated variable method to solve the field control equations for each layer in the magnetic field. This method can transform the model from a three-dimensional disc structure to a form in a two-dimensional Cartesian coordinate system, which has the characteristics of simple solution and more accurate results. Wang and Lin et al. of Southeast University established a two-dimensional general analytical model of the layer model of a permanent magnet coupler with axial flux and then derived the expression of torque by the separated variable method, taking into account the saturation effect of the yoke iron [11]. In order to improve the transmission characteristics of the disc coupler, the structure of the disc coupler was optimized. Halbach arrays, stepped arrays, and curved pole structures have been developed for the magnetization direction, with the conductor disc structure slotted into the core or air. The results of Razavi's [12] study show that slotted copper conductor discs can increase the torque density by more than 50%. However, at this point, the layer modeling method with continuity assumptions does not satisfy the discontinuous eddy current fields or the magnetic field quantities. In this case, the subdomain analytical method is more effective in dealing with discontinuous magnetic field problems [13]. In addition, the finite element method based on 3D models can take into account the nonlinearity of the material as well as the complex magnetic field model. However, it needs to be remodeled and solved every time it is analyzed [14], and although the results are accurate, they are time-consuming and affected by the mesh and other related settings, and they are usually used as a validation method for the analytical

model. Therefore, in the early stage of design, the analytical results of the modeling are mainly used for electromagnetic field calculation and design.

It can be seen that the disc-type permanent magnet coupler structure with an adjustable air gap between the conducting copper disc and its back iron has not yet been studied in the relevant literature. In this paper, firstly, the layer model of this type of disc-type permanent magnet coupler structure is established, and then the equations of the torque characteristics and axial force characteristics are solved by the method of separating variables for this model. Finally, the axial force, torque, and slip characteristics of this permanent magnet coupler structure are investigated by using the three-dimensional finite element method in comparison with the analytical method.

2. Structure and Operation Principles of Permanent Magnet Eddy Current Switching Seal

A switching seal based on permanent magnet drive technology is shown in Figure 2, including an outer rotor structure, an axial force permanent magnet drive structure, and two mechanical seal structures. The left flange (2) and the right flange (8) of the outer rotor structure are bolted together; the axial force permanent magnet drive structure includes a conductor disc assembly and a magnet disc assembly; the conductor disc assembly includes a copper disc (7) and a conductor disc backplane (6), which are fixed to the right flange to achieve the function of rotating together with it, and the magnet disc assembly includes a magnet disc backplane (3), a permanent magnet array (5), and a magnetic holding disc (4), which are achieved by the profile shaft structure, restriction of rotational freedom, and the ability to move axially under axial force.
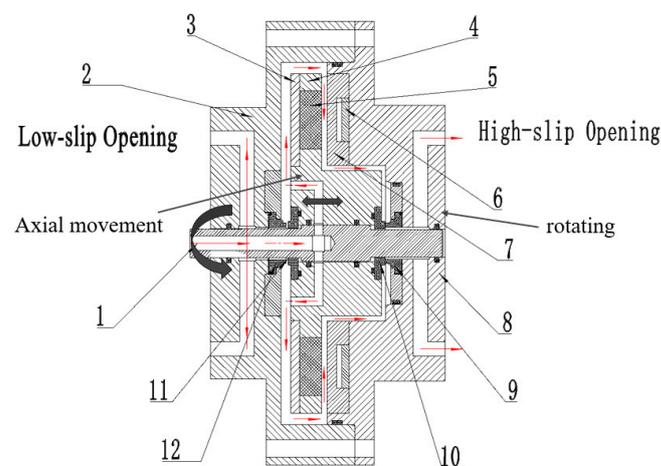
Figure 2. Permanent magnet eddy current drive-switching seal structure (1. water inlet, 2. left flange, 3. magnetic disc backplane, 4. magnetic holding disc, 5. permanent magnet array, 6. conductor disc backplane, 7. copper disc, 8. right flange, 9. right dynamic ring, 10. right stationary ring, 11. left stationary ring, 12. left dynamic ring).

First of all, the two working conditions of the switching seal are defined: when the right seal is closed and the left seal is open, the pressure medium is led to the expansion cylinder of the transverse retractable cutting drum by the inlet port, which is called the cylinder working condition; when the left seal is closed and the right seal is open, the pressure medium is led to the inner spray water distribution seal of the transverse retractable cutting drum by the water inlet, which is called the inner-spraying condition.

The operation of the switching seal is realized by the axial force between the conductor disc assembly and the magnet disc assembly; it consists of two parts: the axial attraction of the conductor disc backplane on the permanent magnet, and the axial repulsion of the permanent magnet by the induced magnetic field generated when the copper disc was cutting. At low slip, the axial attraction of the conductor disc backplane to the permanent

magnet array plays a dominant role, and this attraction keeps the switching seal in the cylinder working condition. When the slip increases, the axial repulsion of the copper disc to the permanent magnet array plays a dominant role, and the repulsion overcomes the medium pressure and attraction, switching the seal to the inner-spraying condition. When the slip decreases, the axial attraction once again plays a dominant role, and the attraction overcomes the medium pressure in the internal spray condition, restoring the cylinder working condition. The working process of the reversing seal is reflected in the hysteresis characteristic. The material and structural parameters are detailed in Table 1.

Table 1. Switching seal material and structural parameters.

Structure Name	Material	Outer Diameter (mm)	Inner Diameter (mm)	Thickness (mm)
Water inlet	022Cr17Ni12Mo2	20	12	-
Left flange	06Cr19Ni10	360	22	70
Magnetic disc backplane	45#	280	110	6
Magnetic holding disc	06Cr19Ni10	280	50.6	12
Permanent magnet array	NdFeB35	240	160	12
Conductor disc backplane	45#	240	160	5
Copper conductor	TU2	280	50	15
Right flange	06Cr19Ni10	360	20	65
Right dynamic ring	Nitrile rubber	28	22	5
Right stationary ring	Filled with PTFE resin	30	20.5	5.5
Left dynamic ring	Silicon carbide	26	22	4
Left stationary ring	M106 K	28	21	5.5

In order to study this type of switching mechanical seal with a permanent magnet eddy current transmission structure, the drive characteristics of the permanent magnet eddy current structure should be studied first. The 3D model of this permanent magnet eddy current structure is shown in Figure 3.
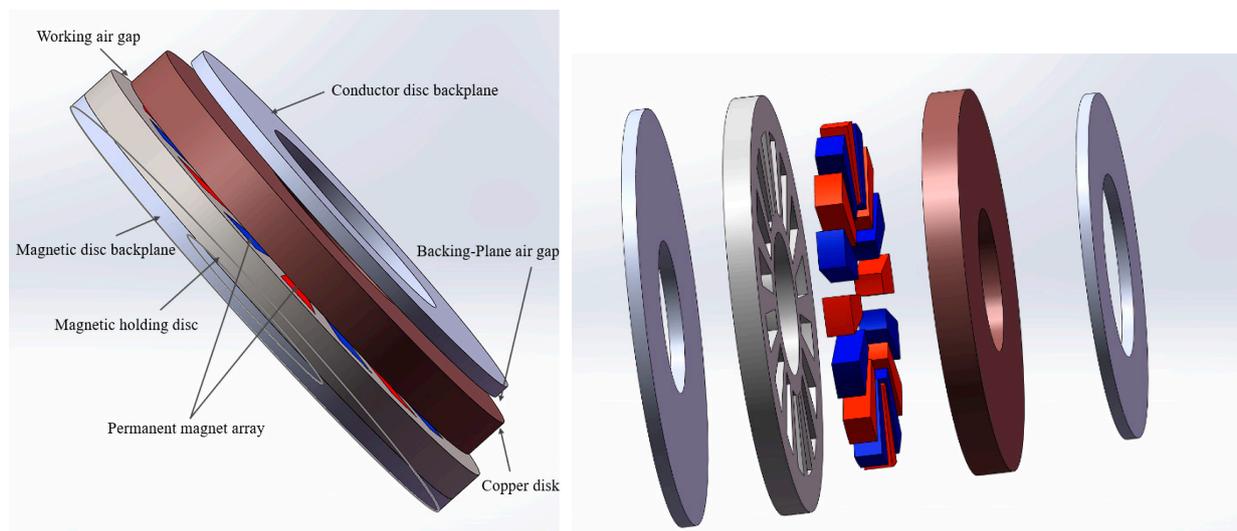
Figure 3. Three-dimensional (3D) permanent magnet eddy current structure for switching mechanical seal.

Figure 4 shows the 2D model of the permanent magnet drive structure. The 2D model can better reflect the geometric parameters of the permanent magnet drive structure. The geometric parameters of the model include the inner diameter of the permanent magnet, d_{pi}; the outer diameter of the permanent magnet, d_{po}; the diameter of the distribution circle of the permanent magnet, d_{avg}; and the inner diameter of the copper disc, d_{ri}; the outer diameter of the copper disc, d_{ro}; a is the thickness of the magnet disc backing iron, b-a is

the axial thickness of the permanent magnet array, δ_1 is the thickness of the working air gap and has the value c-b, d-c is the axial thickness of the copper disc, δ_2 is the thickness of the backplane air gap and has the value e-d, and f-e is the thickness of the backplane of the conductor disc.
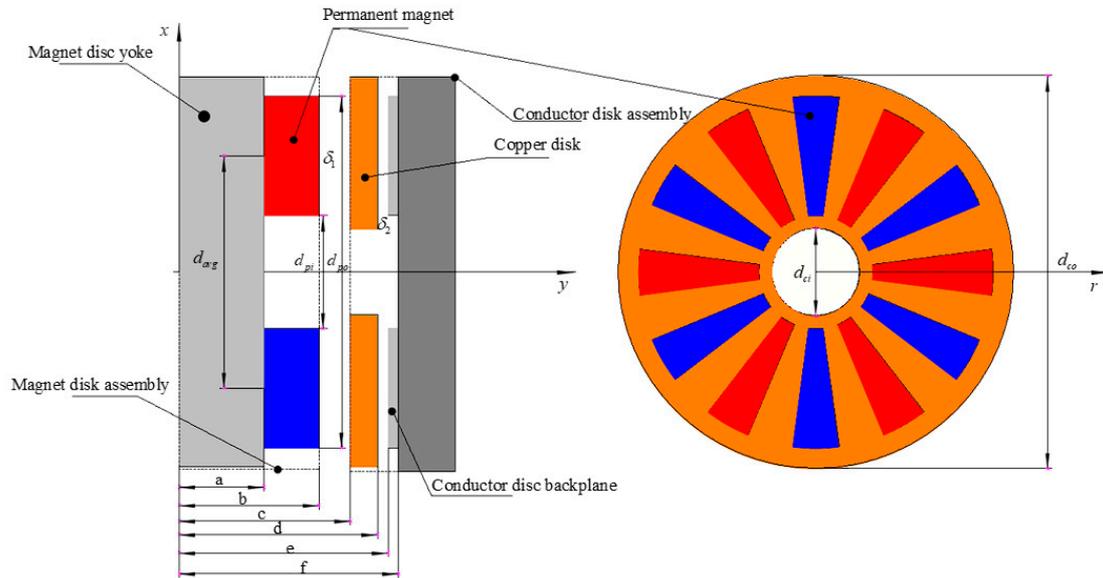
Figure 4. Permanent magnet drive structure for switches.

The structural parameters and performance parameters of the permanent magnet eddy current structure are shown in Tables 2 and 3.

Table 2. Structural parameters of permanent magnet coupling device.

Structural Parameters	Symbolic	Value
Permanent magnet inner diameter	d_{pi}	160 mm
Permanent magnet outer diameter	d_{po}	240 mm
Permanent magnet distribution circle diameter	d_{avg}	200 mm
Permanent magnet pole pair number	p	12
Permanent magnet duty ratio	α	0.5
Copper disc inner diameter	d_{ci}	150 mm
Copper disc outer diameter	d_{co}	250 mm
Working air gap	δ_1	2 mm~10 mm
Backplane air gap	δ_2	0 mm~10 mm
Difference in rotational speed	n	0~1500 rpm

Table 3. Permanent magnet coupling device material properties.

Definition	Symbolic	Value
Vacuum permeability	μ_0	$4\pi \times 10^{-7}$ H/m
Relative permeability of magnet disc backplane and conductor backplane	$\mu_1\mu_6$	2000
Relative permeability of copper	μ_4	0.999991
Relative permeability of air	$\mu_3\mu_5$	1
Relative permeability of permanent magnet	μ_2	1.0997785406
Permanent magnet remanence	B_r	1.22 T
Relative coercivity of permanent magnet	H_c	-8.9×10^5 A/m
Conductivity of copper	σ_4	5.7×10^7 S/m
Conductivity of magnet disc backplane and conductor backplane	$\sigma_1\sigma_6$	2.0×10^7 S/m

3. Modeling and Analysis of Permanent Magnet Eddy Current Structures

3.1. Model and Assumptions

The structure of the permanent magnet drive of the switching seal is shown in Figures 2 and 3. The magnet disc assembly consists of permanent magnets, a stainless steel frame, and the backplane of the magnet disc, with axial movement. Permanent magnets with north–south pole alternation are axially magnetized in a fan-shaped distribution along the circumference. The conductor disc assembly consists of the copper disc and the conductor disc backplane. There is a second air gap between the copper disc and its backplane, which is called the backplane air gap. The holding discs of the conductor disc assembly and magnet disc assembly consist of austenitic stainless steel that is not magnetically conductive and is intended to minimize the influence of other metal parts that may be ferromagnetic on the permanent magnet drive structure.

The structure model of the permanent magnet drive of the switching seal was unfolded along the circumferential direction into a linear model, and the model was truncated axially, resulting in a two-dimensional linear model in Cartesian coordinates (Figure 5). The transformed 2D linear model can be divided into six different layers:

Layer 1: Magnet disc backplane layer;
Layer 2: Permanent magnet array layer;
Layer 3: Working air gap layer;
Layer 4: Copper layer;
Layer 5: Backplane air gap layer;
Layer 6: Conductor disc backplane layer.
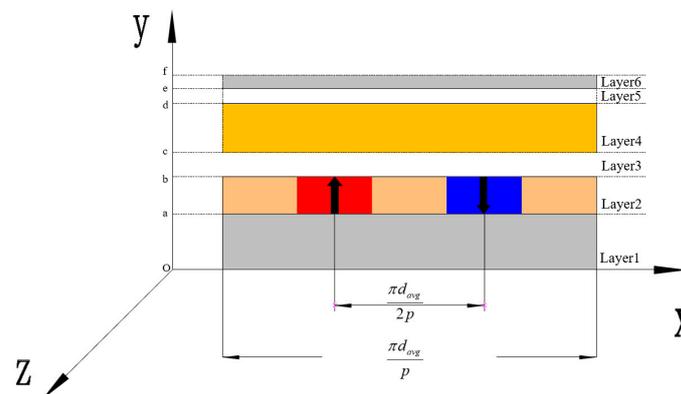
Figure 5. Two-dimensional (2D) linear hierarchical model of a permanent magnet coupling device in a right-angle coordinate system.

To simplify the calculation process and facilitate research, the following assumptions are made:

Only consider the z-component of the eddy current and assume that the z-component of the eddy current is correlated with the x- and y-directions. This is because only the z-component of the eddy current contributes to the drive device.

Each layer is homogeneous, with consistent material properties, and the electromagnetic field in the air regions outside the magnet disc backplane layer and the conductor disc backplane layer is not considered.

Neglect curvature errors caused by coordinate system transformations.

The model has natural periodic boundary conditions along the x-direction, with the period determined by the distance between the poles of the permanent magnet.

The backplane on the conductor disc assembly has finite permeability and non-zero conductivity. Eddy current effects of this layer should be considered in the layer model.

The displacement current in the conductor is ignored.

Analysis is conducted based on the relative velocity between the conductor disc assembly and the magnet disc assembly; v can be represented as follows:

$$v = \frac{\pi n d_{avg}}{60} \qquad (1)$$

where n represents the relative velocity between the conductor disc and the magnet disc (rpm), while d_{avg} represents the average diameter of the permanent magnet (mm).

The subsequent establishment of the mathematical model for the electromagnetic field will be based on the above assumptions.

3.2. Model Analysis and Control Equations

The basic magnetic field equation of the permanent magnet eddy current structure is expressed in terms of the magnetic vector [15] as Poisson Equation (2). Its derivation is shown in Appendix A:

$$\nabla^2 \mathbf{A}_k = \frac{\partial^2 A_k}{\partial x^2} + \frac{\partial^2 A_k}{\partial y^2} = -\mu_0 \mu_k J_k \qquad (2)$$

where $\mathbf{A}_k$ represents the magneticmvector of Layer k. μ_0 represents the vacuum permeability, with a value of $4\pi \times 10^{-7}$ H/m. μ_k represents the relative magnetic permeability of Layer k. J_k represents the current density in Layer k.

Layer 2 has a magnetic field source but no current, and the magnetization intensity $\mathbf{M}_2 = \mathbf{M}_r$. The magnetic field intensity in the x-direction and y-direction is

$$\mathbf{B}_2 = \begin{bmatrix} B_{2,x} \\ B_{2,y} \end{bmatrix} = \mu_0 \mu_2 \begin{bmatrix} H_{2,x} \\ H_{2,y} \end{bmatrix} + \mu_0 \begin{bmatrix} 0 \\ M_r \end{bmatrix} \qquad (3)$$

When a specific type of permanent magnet material is selected, the relationship between the magnetization intensity of the permanent magnet can be expressed as follows:

$$\mathbf{M}_r = \frac{\mathbf{B}_r}{\mu_0} \qquad (4)$$

where $\mathbf{B}_r$ is the remanence of the permanent magnet, as shown in Figure 6, where $\mathbf{B}_r$ along the x-direction in a rectangular wave distribution in the permanent magnet and outside the permanent magnet is equal to $B_r(-B_r)$ and 0, respectively, and B_r expands the Fourier series as follows:

$$B_r(x) = \sum_n B_{r,n} e^{imx} \ (n = 1, 3, 5 \ldots) \qquad (5)$$

$$m = \frac{\pi}{\tau_p n} \qquad (6)$$

where τ_p is the pole distance, $\tau_p = \frac{\pi d_{avg}}{2p}$
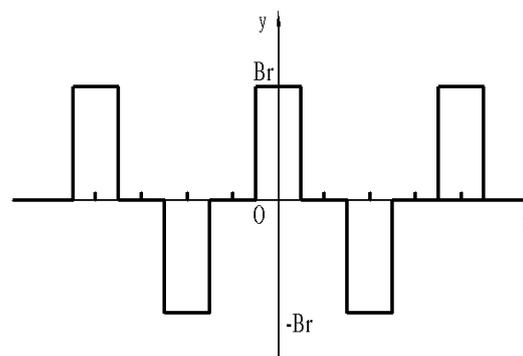
Figure 6. Magnetization distribution along the x−direction.

Thus,

$$\nabla \times \mathbf{B}_2 = \nabla \times (\mathbf{H}_2 + \mathbf{M}_r) = \mu_0 \nabla \times \mathbf{M}_r \tag{7}$$

The field control equation satisfied by Layer 2 is

$$\nabla^2 \mathbf{A}_2 = -\mu_0 \nabla \times \mathbf{M}_r = -\nabla \times \mathbf{B}_2 \tag{8}$$

Layers 1, 3, and 5 have no magnetic field sources and no current.

$$\begin{cases} \nabla \times \mathbf{H}_k = \mathbf{J}_k = 0 \\ \mathbf{B}_k = \mu_0 \mathbf{H}_k \end{cases} \tag{9}$$

Layer 1 is the backplane of the magnet disc assembly, which has a velocity of zero with respect to the permanent magnet; Layer 3 and Layer 5 are the air gap regions, with a conductivity of zero and no current. Thus, the equations that regulate the electromagnetic field within these regions are as follows:

$$\nabla^2 \mathbf{A}_1 = \frac{\partial^2 A_1}{\partial x^2} + \frac{\partial^2 A_1}{\partial y^2} = 0 \tag{10}$$

$$\nabla^2 \mathbf{A}_3 = \frac{\partial^2 A_3}{\partial x^2} + \frac{\partial^2 A_3}{\partial y^2} = 0 \tag{11}$$

$$\nabla^2 \mathbf{A}_5 = \frac{\partial^2 A_5}{\partial x^2} + \frac{\partial^2 A_5}{\partial y^2} = 0 \tag{12}$$

Layer 4 and Layer 6 have no magnetic field sources but have current flowing through them.

$$\begin{cases} \nabla \times \mathbf{H}_4 = \mathbf{J}_4 \\ \mathbf{J}_4 = \sigma_4 \mathbf{E}_4 \\ \nabla \times \mathbf{E}_4 = -\frac{\partial \mathbf{B}_4}{\partial t} = -\frac{d\mathbf{B}_4}{dx}\frac{dx}{dt} = -\frac{d\mathbf{B}_4}{dx}v \\ \mathbf{B}_4 = \mu_0 \mu_4 \mathbf{H}_4 \end{cases} \tag{13}$$

$$\begin{cases} \nabla \times \mathbf{H}_6 = \mathbf{J}_6 \\ \mathbf{J}_6 = \sigma_6 \mathbf{E}_6 \\ \nabla \times \mathbf{E}_6 = -\frac{\partial \mathbf{B}_6}{\partial t} = -\frac{d\mathbf{B}_6}{dx}\frac{dx}{dt} = -\frac{d\mathbf{B}_6}{dx}v \\ \mathbf{B}_6 = \mu_0 \mu_6 \mathbf{H}_6 \end{cases} \tag{14}$$

Solving the relative velocity with Equation (1), the field control equations satisfied by Layer 4 and Layer 6 are

$$\nabla^2 \mathbf{A}_4 = \frac{\partial^2 A_4}{\partial x^2} + \frac{\partial^2 A_4}{\partial y^2} = \frac{n\pi \mu_0 \mu_4 \sigma_4 d_{avg}}{60} \frac{d\mathbf{A}_4}{dx} \tag{15}$$

$$\nabla^2 \mathbf{A}_6 = \frac{\partial^2 A_6}{\partial x^2} + \frac{\partial^2 A_6}{\partial y^2} = \frac{n\pi \mu_0 \mu_6 \sigma_6 d_{avg}}{60} \frac{d\mathbf{A}_6}{dx} \tag{16}$$

At this point, the general solution for the magnetic field of this type of disc-shaped permanent magnet coupling device is Equation (17) [16]. The detailed calculation process is presented in Appendix B

$$\begin{cases} \mathbf{A}_1(x,y) = (C_1 e^{my} + D_1 e^{-my}) e^{imx} \\ \mathbf{A}_2(x,y) = \left(C_2 e^{my} + D_2 e^{-my} - \frac{j\mathbf{B}_r}{m}\right) e^{imx} \\ \mathbf{A}_3(x,y) = (C_3 e^{my} + D_3 e^{-my}) e^{imx} \\ \mathbf{A}_4(x,y) = (C_4 e^{\lambda_1 y} + D_4 e^{-\lambda_1 y}) e^{imx} \\ \mathbf{A}_5(x,y) = (C_5 e^{my} + D_5 e^{-my}) e^{imx} \\ \mathbf{A}_6(x,y) = (C_6 e^{\lambda_2 y} + D_6 e^{-\lambda_2 y}) e^{imx} \end{cases} \tag{17}$$

where C_i and D_i depend on the boundary conditions. The definitions of λ_1 and λ_2 are as follows [17]:

$$\lambda_1 = \sqrt[4]{m^4 + (m\mu_0\mu_4\sigma_4 v)^2} e^{j\frac{1}{2}\arctan\left(\frac{\mu_0\mu_4\sigma_4 v}{m}\right)} \tag{18}$$

$$\lambda_2 = \sqrt[4]{m^4 + (m\mu_0\mu_6\sigma_6 v)^2} e^{j\frac{1}{2}\arctan\left(\frac{\mu_0\mu_6\sigma_6 v}{m}\right)} \tag{19}$$

3.3. The Boundary Conditions

According to Assumption 2, neglecting the air regions outside the two backplane layers, the boundary conditions are as follows:

$$\begin{cases} \left.\dfrac{\partial \mathbf{A}_{1n}}{\partial x}\right|_{y=0} = 0 \\[2mm] \left.\dfrac{\partial \mathbf{A}_{6n}}{\partial x}\right|_{y=f} = 0 \end{cases} \tag{20}$$

According to the basic theory of electromagnetic fields, at different interfaces between media, the magnetic field satisfies the continuity of the tangential component of the magnetic field intensity and the normal component of the magnetic induction intensity (satisfying the Dirichlet–Neumann interface conditions).

$$\frac{d\mathbf{A}_{kn}}{dx} = \left.\frac{d\mathbf{A}_{(k+1)n}}{dx}\right|_{k=1,2,3,4,5} \tag{21}$$

$$\frac{1}{\mu_k}\frac{d\mathbf{A}_{kn}}{dy} = \left.\frac{1}{\mu_{k+1}}\frac{d\mathbf{A}_{(k+1)n}}{dy}\right|_{k=1,2,3,4,5} \tag{22}$$

Detailed boundary conditions are shown in Appendix C.

3.4. Torque Equation

From the relationship between eddy current density and magnetic flux density, the expression for the eddy current density in the copper conductor disc of the fourth layer of the conductor disc assembly and its backplane of the sixth layer can be obtained as follows:

$$J_{4z} = -\sigma_4 v\frac{\partial \mathbf{A}_4}{\partial x} = -im\sigma_4 v\left(C_4 e^{\lambda_1 y} + D_4 e^{-\lambda_1 y}\right)e^{imx} \tag{23}$$

$$J_{6z} = -\sigma_6 v\frac{\partial \mathbf{A}_6}{\partial x} = -im\sigma_6 v\left(C_6 e^{\lambda_1 y} + D_6 e^{-\lambda_1 y}\right)e^{imx} \tag{24}$$

Therefore, the average eddy current density in the copper conductor disc and the backplane of the conductor disc assembly can be expressed as follows:

$$J_{4avg} = \frac{\int_c^d \int_{-\frac{\tau_p}{2}}^{\frac{\tau_p}{2}} J_{4z}\,dx\,dy}{\tau_p(d-c)} \tag{25}$$

$$J_{6avg} = \frac{\int_e^f \int_{-\frac{\tau_p}{2}}^{\frac{\tau_p}{2}} J_{6z}\,dx\,dy}{\tau_p(f-e)} \tag{26}$$

The eddy current losses in the copper conductor disc and the backplane of the conductor disc assembly can be calculated from the eddy current density as follows:

$$P_{4\omega} = \frac{L_4}{\sigma_4}\iint\limits_{Layer4} \left|J_{4avg}^{\ 2}\right| dx\,dy \tag{27}$$

$$P_{6\omega} = \frac{L_6}{\sigma_6} \iint\limits_{Layer6} \left| J_{6avg}^2 \right| dxdy \tag{28}$$

Therefore, the analytical expression for the output torque of the entire conductor disc assembly is

$$T = \frac{P_{4\omega} + P_{6\omega}}{\omega} \tag{29}$$

In the conductive layer of the conductor disc assembly, the induced eddy currents exist in a closed-loop form within the conductive layer. However, only the eddy currents flowing radially will affect the torque of the permanent magnet eddy current structure. Therefore, Equation (30) neglects the circumferential flow of eddy currents outside the region directly facing the permanent magnet and the conductor disc. The actual eddy current direction of the conductor disk is shown in Figure 7. As a result, the calculated torque deviates from the actual situation. Correcting for the three-dimensional end effects can make the model's calculation results more consistent with reality. The R-N correction factor provides a correction factor for considering the three-dimensional end effects, improving the accuracy of torque calculation in the model [18].

$$k_s = 1 - \frac{\tanh\left(\frac{\pi L_p}{2\tau_p}\right)}{\frac{\pi L_p}{2\tau_p}\left\{1 + \tanh\left(\frac{\pi L_p}{2\tau_p}\right)\tanh\left(\frac{\pi(L_c - L_p)}{2\tau_p}\right)\right\}} \tag{30}$$

where L_p is the radial length of the permanent magnet, $L_p = (d_{po} - d_{pi})/2$; L_c is the radial width of the copper disc, $L_c = (d_{co} - d_{ci})/2$.
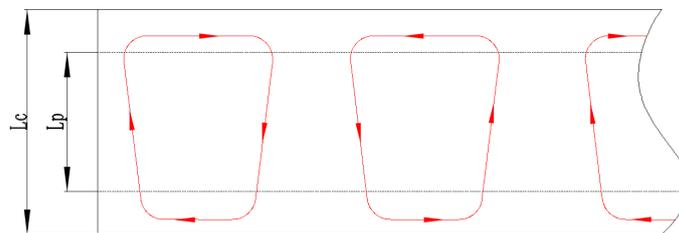
Figure 7. The actual eddy current direction of the conductor disk.

Therefore, the corrected output torque of the entire conductor disc assembly is

$$T_o = k_s T \tag{31}$$

3.5. Axial Force Equation

From the relationship between magnetic flux density and magnetic field intensity, the expression for the magnetic flux density in the copper conductor disc and the backplane of the conductor disc assembly can be obtained as follows:

$$\begin{cases} B_{4x} = \frac{\partial A_4}{\partial y} = \lambda_1 e^{imx}\left(C_4 e^{\lambda_1 y} - D_4 e^{\lambda_1 y}\right) \\ B_{4y} = -\frac{\partial A_4}{\partial x} = -im e^{imx}\left(C_4 e^{\lambda_1 y} + D_4 e^{-\lambda_1 y}\right) \end{cases} \tag{32}$$

$$\begin{cases} B_{6x} = \frac{\partial A_6}{\partial y} = \lambda_2 e^{imx}\left(C_6 e^{\lambda_2 y} - D_6 e^{\lambda_2 y}\right) \\ B_{6y} = -\frac{\partial A_6}{\partial x} = -im e^{imx}\left(C_6 e^{\lambda_2 y} + D_6 e^{-\lambda_2 y}\right) \end{cases} \tag{33}$$

At this point, the axial force acting on the magnet disc can be expressed using the Maxwell stress tensor method. The axial force can be represented as follows:

$$F = \oiint\limits_{S_4} \overset{\leftrightarrow}{T_4} \cdot ds + \oiint\limits_{S_6} \overset{\leftrightarrow}{T_6} \cdot ds \tag{34}$$

where S_4 represents the surface surrounding the copper disc, S_6 representsnthe surface surrounding the yoke iron of the conductor disc, and $\overset{\leftrightarrow}{T}$ represents the Maxwell stress tensor at any point on this surface. However, in the electromagnetic field model of the permanent magnet eddy current structure, the current density vector on the surface of the conductor disc has no axial component. Therefore, the expression for the Maxwell stress tensor, after omitting the electric field intensity term, is given by Equation (35) as follows:

$$\overset{\leftrightarrow}{T} = \frac{1}{\mu_0} \begin{bmatrix} B_x^2 - \frac{1}{2}|\mathbf{B}|^2 & B_x B_y & 0 \\ B_y B_x & B_y^2 - \frac{1}{2}|\mathbf{B}|^2 & 0 \\ 0 & 0 & -\frac{1}{2}|\mathbf{B}|^2 \end{bmatrix} \tag{35}$$

According to the tensor operator identity $\oiint_s \mathrm{d}s = \iiint_V \nabla \mathrm{d}V$, the axial force acting on the magnet disc can be expanded as follows:

$$F = \iiint_{V_1} \nabla \overset{\leftrightarrow}{T_4} \cdot dV + \iiint_{V_2} \nabla \overset{\leftrightarrow}{T_6} \cdot dV \tag{36}$$

The axial force in the y-direction can be expressed as follows:

$$F_y = F_{y_4} + F_{y_6} \tag{37}$$

$$F_{y4} = \int_c^d \int_0^{\pi d_{avg}} \left(\frac{1}{\mu_0} \frac{\partial (B_{4y} B_{4x})}{\partial y} + \frac{1}{\mu_0} \frac{\partial \left(B_{4y}^2 - \frac{1}{2}|\mathbf{B}_4|^2 \right)}{\partial y} \right) dxdy \tag{38}$$

$$F_{y6} = \int_e^f \int_0^{\pi d_{avg}} \left(\frac{1}{\mu_0} \frac{\partial (B_{6y} B_{6x})}{\partial y} + \frac{1}{\mu_0} \frac{\partial \left(B_{6y}^2 - \frac{1}{2}|\mathbf{B}_6|^2 \right)}{\partial y} \right) dxdy \tag{39}$$

4. Finite Element Analysis of the Electromagnetic Field in Permanent Magnet Eddy Current Structures

In order to compare the accuracy of analytical results, and in accordance with the design requirements of mechanical seal compensation mechanisms, considering the space constraints inside the truncated roller, the structural design was first completed based on the principle of coordination between the permanent magnet structure and the size of the water inlet shaft seal. Secondly, referring to the research results of Mengyao Wang [19], it is known that the torque and axial force affecting the transmission of the permanent magnet drive mainly include the axial air gap length and slip. Magnetization strength is related to the thickness of the permanent magnet and the thickness of the copper plane. Based on this, the following assumptions and simplifications are made for the establishment and analysis of the finite element model:

1. The permanent magnet material is neodymium iron boron, uniformly magnetized along the axial direction, and the demagnetization caused by thermal conduction due to eddy current effects is not considered.
2. The magnetic conductor is an isotropic material.
3. Only components related to electromagnetic effects in the model are considered, namely, the permanent magnet, copper conductor disc, conductor disc backplane, and the magnetic shielding effect of the conductor disc yoke iron. The electromagnetic effects of other metal components are neglected, and their structures are treated as air.

4.1. Finite Element Model Meshing Results

The finite element mesh model of the permanent magnet eddy current drive mechanism after irrelevant inspection is shown in Figure 8.
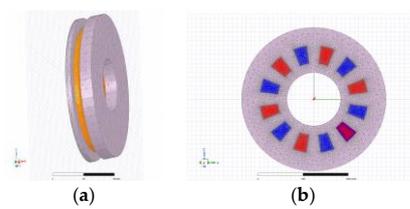
Figure 8. Finite element mesh division model of permanent magnet eddy current structure: (**a**) Finite element mesh of permanent magnet eddy current structure. (**b**) Finite element mesh of magnet disc.

4.2. Static Magnetic Field Results of the Permanent Magnet Eddy Current Structure

When the relative speed is 0 r/min, the magnetic flux density on the front and back of the conductor disc assembly, as obtained from the simulation, is shown in Figure 9. At this time, the permanent magnet drive switch is in a stationary position, and the position of the conductor disc assembly relative to the magnet disc assembly is fixed. The magnetic field in the air gap is kept stable by the residual magnetism of the permanent magnet, and the main axial force on the magnet disc assembly is exerted by the conductor disc backplane. From the static magnetic field analysis, it can be observed that the size of the air gap is an important factor affecting the magnetic field intensity. Under the static conditions of the cylinder, a 2 mm air gap allows the magnetic field to pass through a relatively narrow gap, resulting in a large magnetic flux, with a magnetic field intensity of 0.613 T on the surface of the conductor disc. However, under the 4 mm air gap of the spray condition, the magnetic field intensity is relatively lower at 0.570 T due to increased magnetic leakage in the air gap and on the surface of the permanent magnet. From Figure 10c, it can also be observed that the arrangement of the stainless steel yoke iron on the conductor disc provides good isolation from other metal materials.
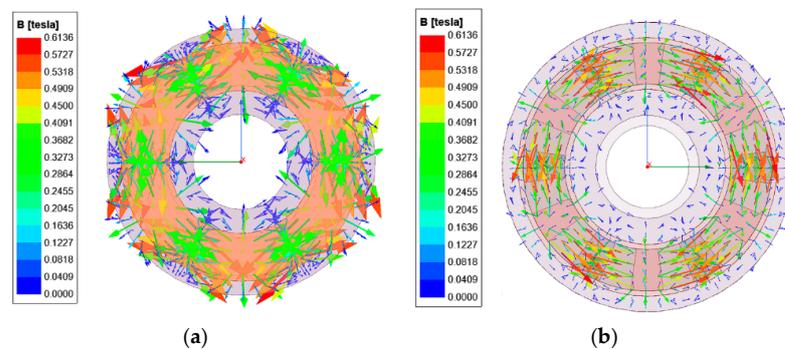
Figure 9. Magnetic flux density contour map on the surface of the conductor disc with a 2 mm working air gap under static conditions: (**a**) On the front surface of the conductor disc. (**b**) On the back surface of the conductor disc.
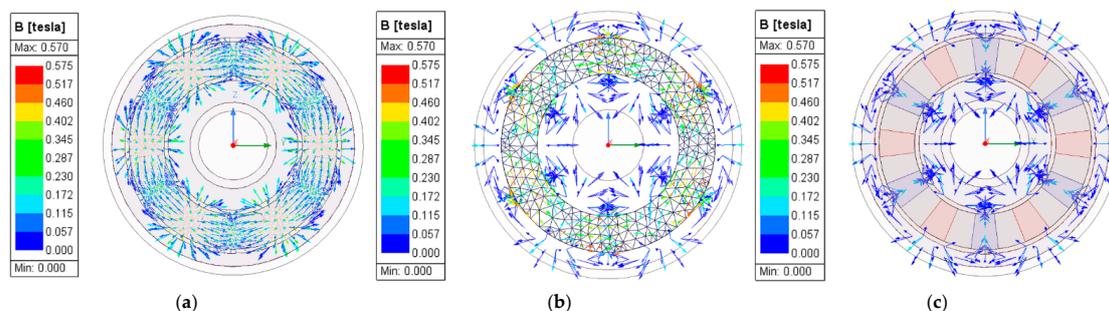
Figure 10. Magnetic flux density contour map on the surface of the conductor disc with a 4 mm working air gap under static conditions: (**a**) Flux density of copper disc. (**b**) Flux density of conductor disc backplane. (**c**) Flux density of conductor disc frame.

4.3. Transient Magnetic Field Results of the Permanent Magnet Eddy Current Structure

When the relative speed is 20 rpm, the magnetic flux density on the front and back of the conductor disc assembly, as obtained from the simulation under two different conditions, is shown in Figures 11 and 12. The magnetic flux in the air gap region on the surface of the conductor disc within the permanent magnet eddy current structure is attenuated compared to the static case. This is because, under static conditions, the magnetic flux can fully pass through the air gap region, resulting in a higher magnetic field intensity in the air gap. However, as the relative speed increases, as shown in Figure 13, the magnetic flux in the working air gap region is affected by the locally induced magnetic field of eddy currents, and the two magnetic fields superimpose, resulting in a decrease in magnetic flux and, subsequently, a decrease in magnetic field intensity.

(a)

(b)
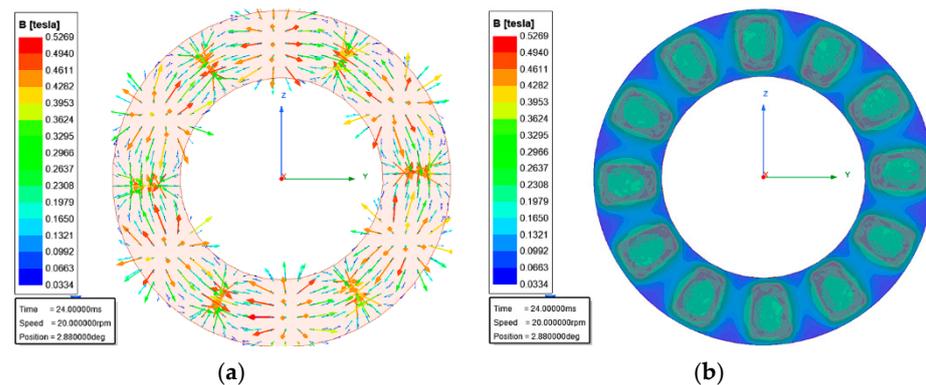
Figure 11. Magnetic flux density map on the surface of the conductor disc with a 2 mm working air gap under transient conditions (20 rpm): (**a**) Line of magnetic flux. (**b**) Magnetomimetic map.

(a)

(b)
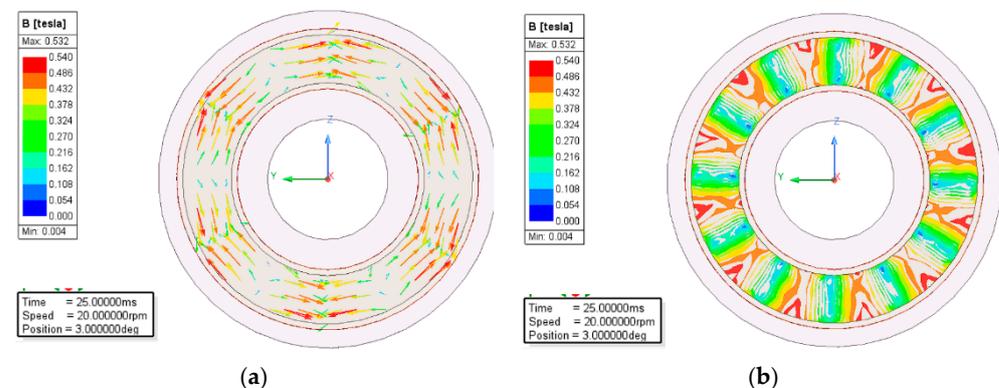
Figure 12. Magnetic flux density map on the surface of the conductor disc under transient conditions with a 4 mm working air gap (20 rpm): (**a**) Line of magnetic flux. (**b**) Magnetomimetic map.

By comparing the induced current density on the surface of the copper conductor disc at 20 rpm in Figure 14a and 120 rpm in Figure 14b with a working air gap of 4 mm, it can be observed that with increasing speed, the induced current density in the copper disc increases rapidly, possibly due to the eddy current effect. Under low-slip conditions, as the speed increases, the induced electromotive force in the copper disc increases, stimulating more eddy currents. These eddy currents lead to a significant increase in the induced current density in the copper disc, and this nonlinear response may result in a rapid increase in induced current density.
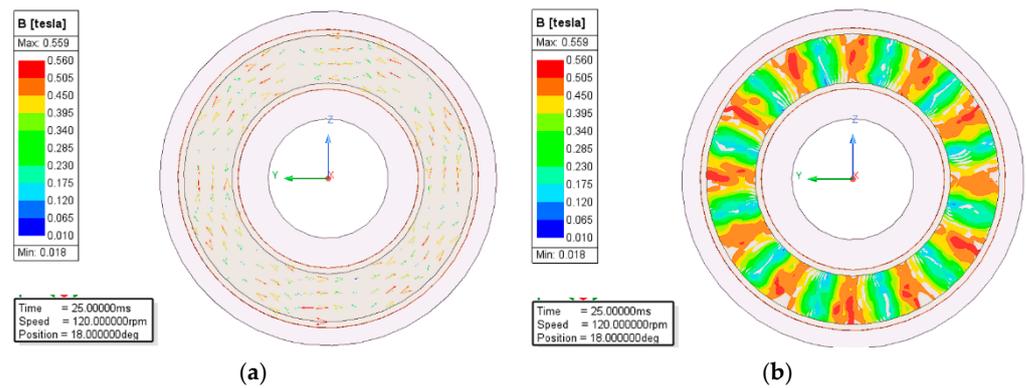
Figure 13. Magnetic flux density map on the surface of the conductor disc under transient conditions with a 4 mm working air gap (120 rpm): (**a**) Line of magnetic flux. (**b**) Magnetomimetic map.
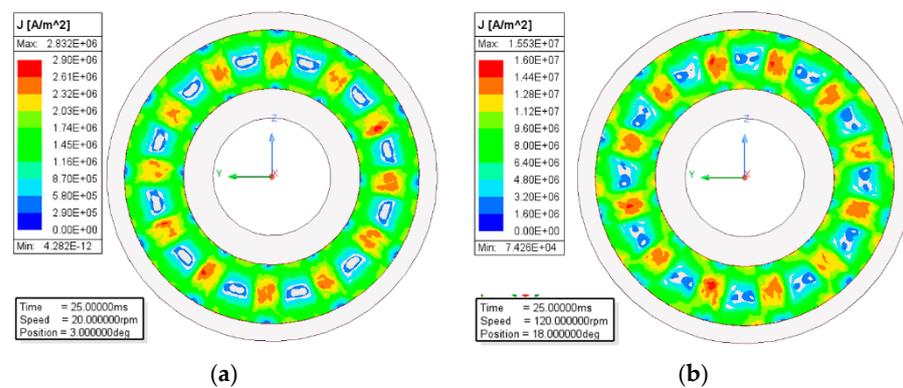
Figure 14. Transient induced current density map on the surface of the copper conductor disc: (**a**) Induced current density at 20 rpm. (**b**) Induced current density at 120 rpm.

4.4. Transmission Characteristics of the Permanent Magnet Eddy Current Structure

From Figures 15 and 16, it can be observed that the overall theoretical curves of the layer model's analytical results are in good agreement with the finite element analysis results in the low-slip region. The predictive results of the analysis and modeling method are more accurate in the low-slip region, but there is a larger error in the region of larger slips. However, the trend of the transmission characteristics is accurate. When cutting coal at low speeds of 20 rpm at the truncation section, the analytical model can be used to calculate the axial force and torque of the permanent magnet eddy current structure, thereby calculating the range of compensating force that can be provided when designing the seal and the switching conditions of the seal.
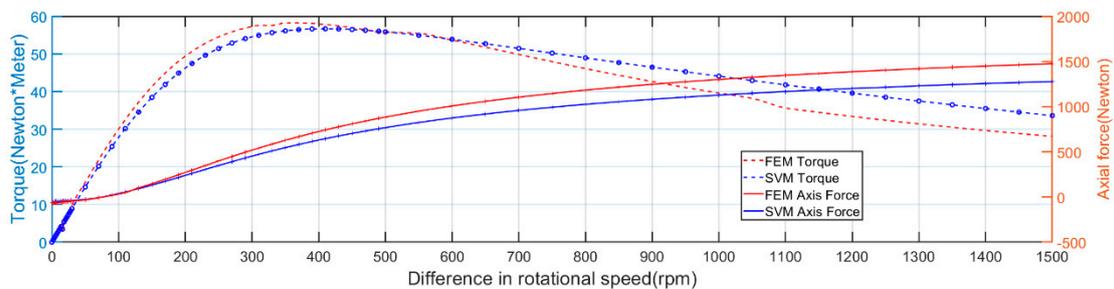
Figure 15. Torque and axial force−slip characteristic curve of the permanent magnet eddy current structure (2 mm).
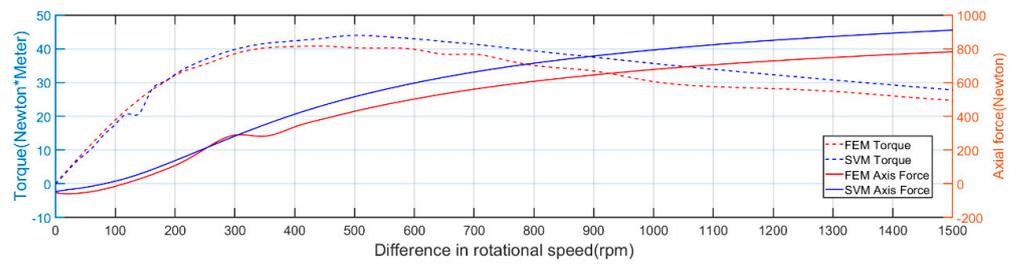
Figure 16. Torque and axial force−slip characteristic curve of the permanent magnet eddy current structure (4 mm).

From Figures 17 and 18, it can be observed that the transmission characteristics of the permanent magnet eddy current switch-type seal are related to the working air gap as follows: as the working air gap increases, the torque transmitted by the permanent magnet eddy current structure rapidly decreases, and the axial force transmitted also decreases accordingly. The initial axial force applied to the magnet disc decreases as the working air gap in-creases.
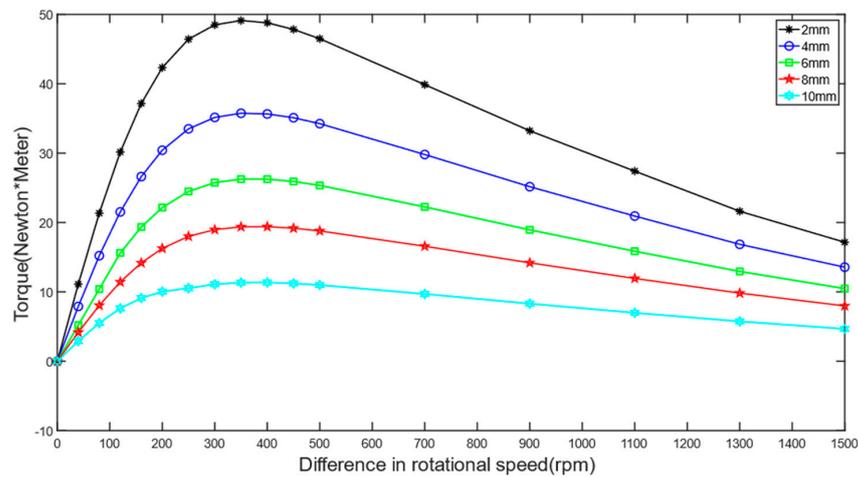
Figure 17. Torque−slip characteristic curve of the permanent magnet eddy current structure (working air gap).
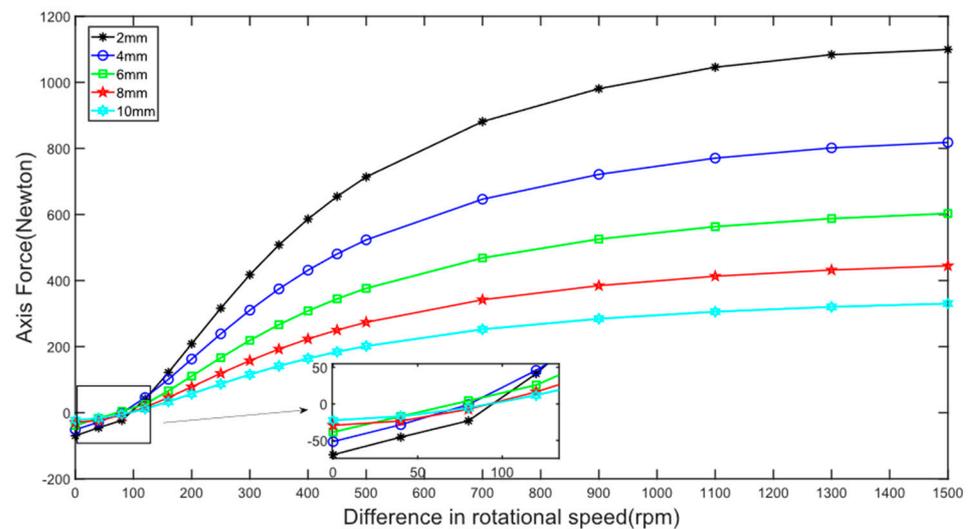
Figure 18. Axial force−slip characteristic curve of the permanent magnet eddy current structure (working air gap).

From Figures 19 and 20, it can be observed that the transmission characteristics of the permanent magnet eddy current structure are related to the backplane air gap as follows: in the low-slip region, as the backplane air gap increases, the rate of increase in torque transmitted by the permanent magnet eddy current structure decreases with increasing slip, and the maximum torque that can be achieved decreases. The initial axial force decreases with increasing backplane air gap, and the rate of increase in axial force with increasing slip decreases. In the high-slip region, the torque and axial force of the permanent magnet eddy current structure are not significantly affected by the thickness of the working air gap, but they depend on the slip speed. This is because, under high-slip conditions, the interaction between the induced magnetic field on the surface of the copper disc in the conductor disc assembly and the magnetic field of the permanent magnet dominates.
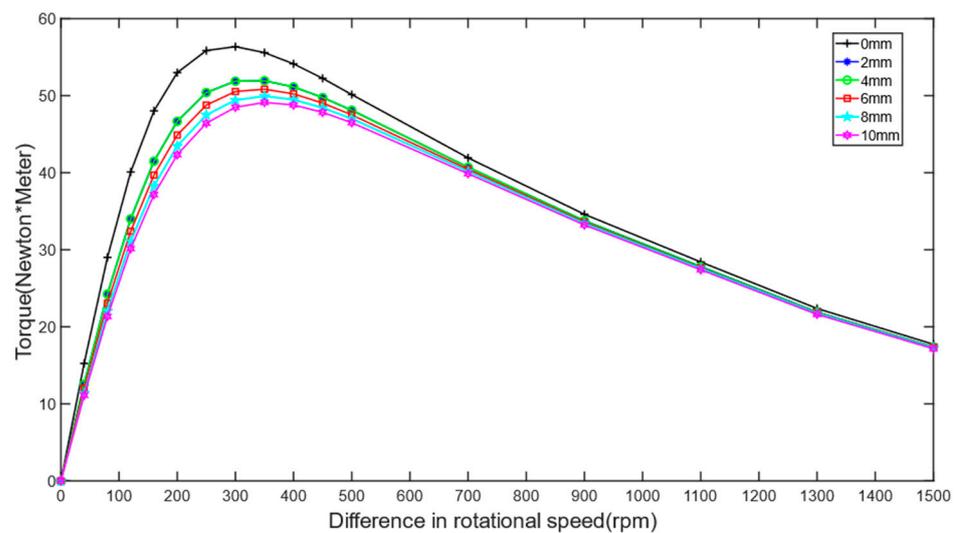
Figure 19. Torque—slip characteristic curve of the disc-type permanent magnet drive device (backplane air gap).
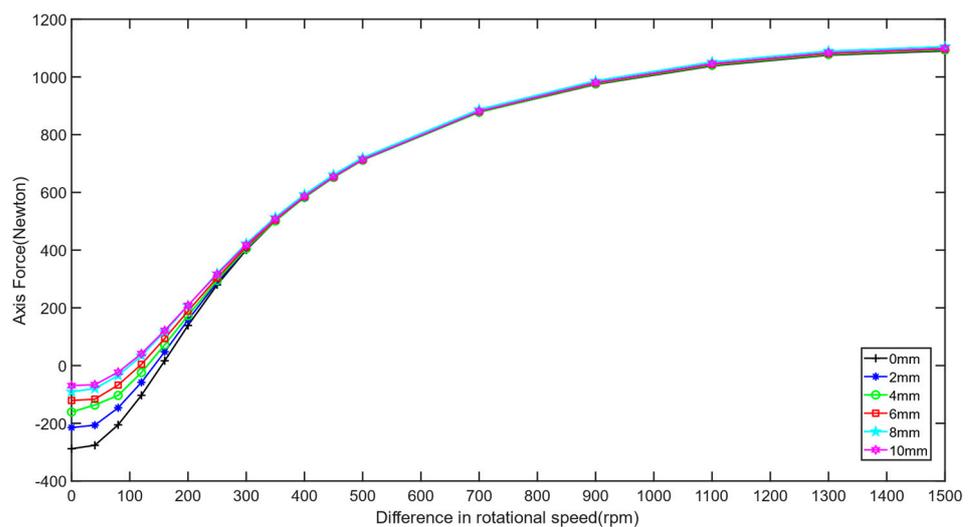
Figure 20. Axial force—slip characteristic curve of the disc-type permanent magnet drive device (backplane air gap).

From Figures 21 and 22, the transmission characteristics of the permanent magnet eddy current structure are not significantly connected to the thickness of the backplane, as follows: when the working air gap is the same as the backing plate air gap, the torque

and axial force communicated by the permanent magnet eddy current structure remain constant as the backplane thickness increases.
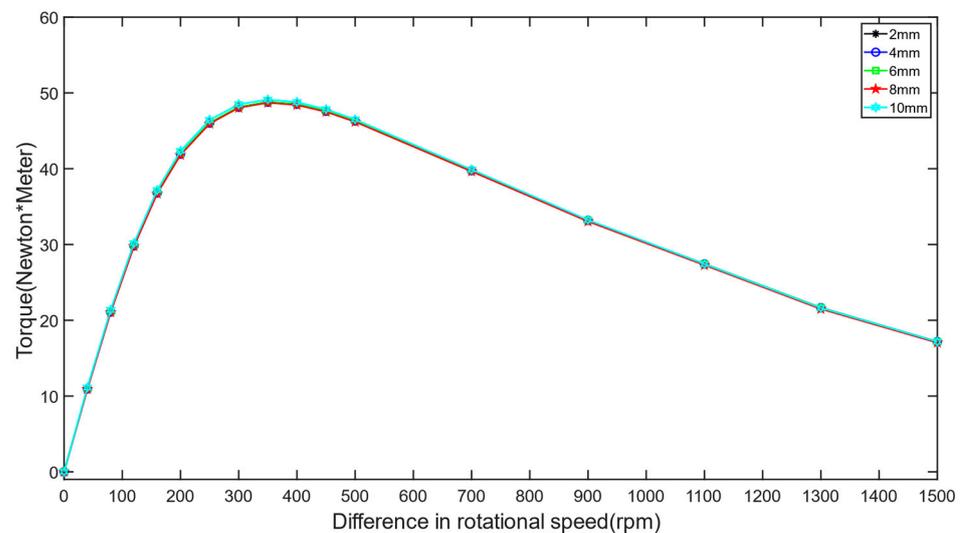
Figure 21. Torque—slip characteristic curve of the permanent magnet eddy current structure vs. backplane thickness.
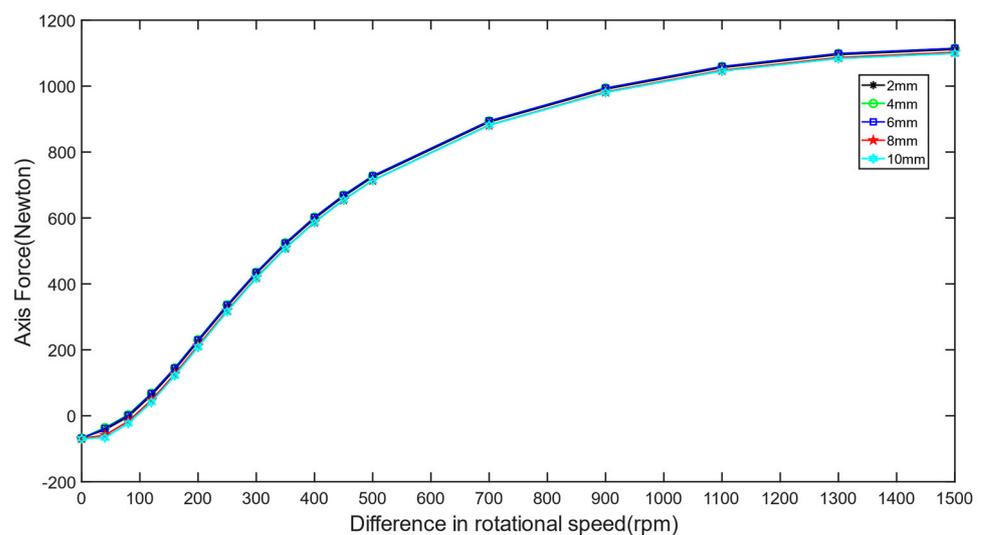
Figure 22. Axial force—slip characteristic curve of the permanent magnet eddy current structure vs. backplane thickness.

Figure 23 shows the relationship between axial force and different conductor disc thicknesses at various backplane air gaps. It can be observed that the axial force applied to the magnet disc is related to the size of the backplane air gap where the conductor disc backplane is situated, and it is not dependent on the thickness of the conductor disc backplane. When the backplane air gap is smaller, the axial force applied to the magnet disc is greater.

Thus, as shown in Figure 24, in the static state, the attraction of the magnet disc assembly by the conductor disc backplane is only related to the thickness of the adjustable air gap, which tends toward 0 as this air gap increases, with the relationship approximated by $F_y = -139.9e^{-0.5389x}$.
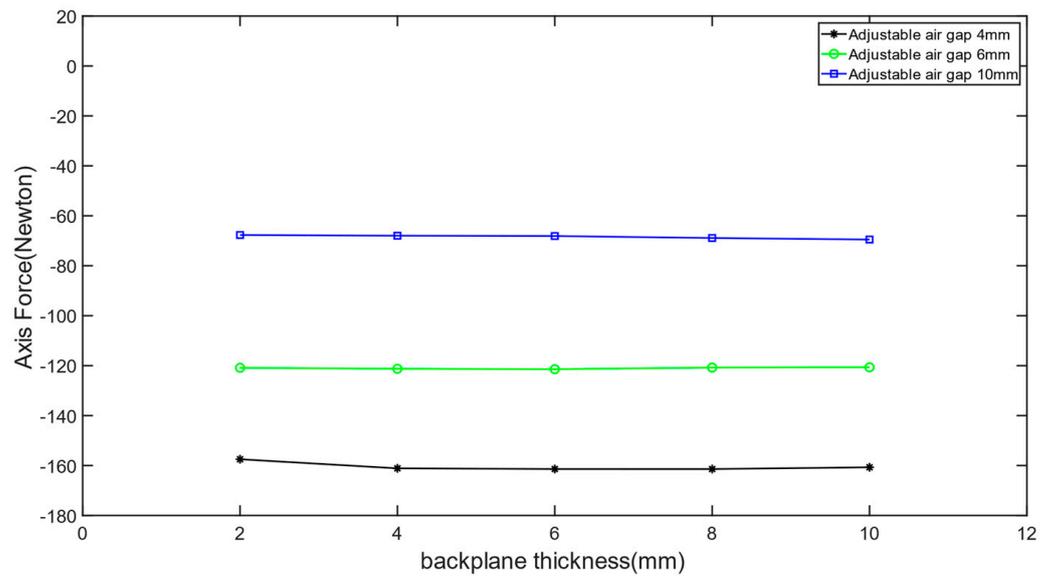
Figure 23. Conductor disc backplane thickness−axial force curve.
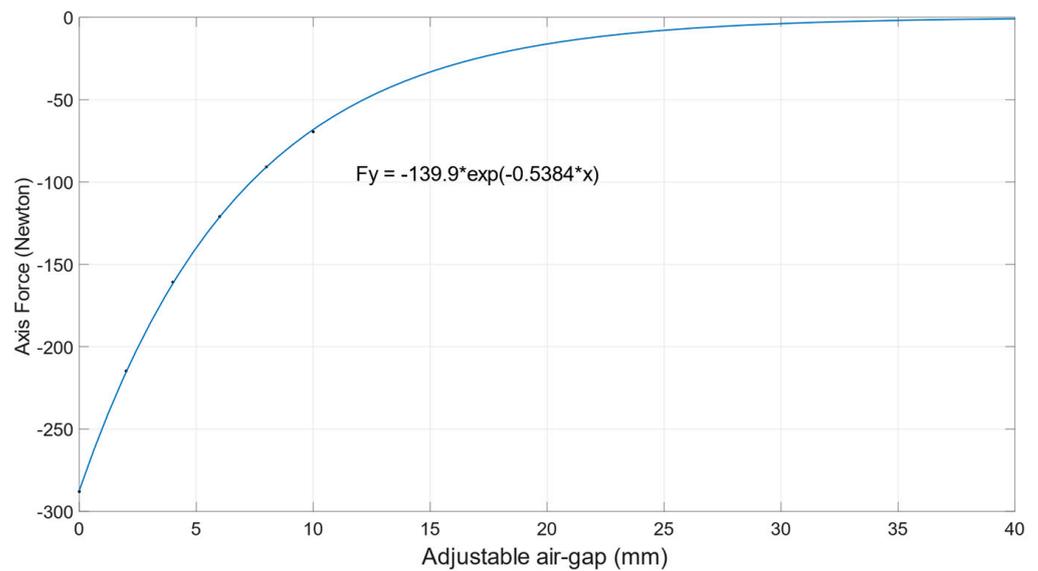
Figure 24. Thickness of the adjustable air gap −axial force curve.

Figures 25 and 26 depict the relationship between axial force, torque, and slip for different conductor disc thicknesses at various backplane distribution circle diameters and backplane widths. It can be observed that, in the high-slip region, the axial force and torque applied to the magnet disc are independent of the structural parameters of the conductor disc backplane. This is because, at high slip, the transmitted axial force and torque mainly come from the induced magnetic field generated by the copper disc in the conductor disc acting on the magnet disc. In the low-slip region, the axial force and torque applied to the magnet disc are related to the area of the magnet disc facing the conductor disc backplane. A larger facing area results in a larger axial force and torque being applied to the magnet disc. Figure 27 represents the axial force generated per unit area of the conductor disc backplane for different distribution circles, where the smaller the total area of the conductor disc backplane, the higher the axial force per unit area—a difference that is not captured by the two-dimensional layer model.
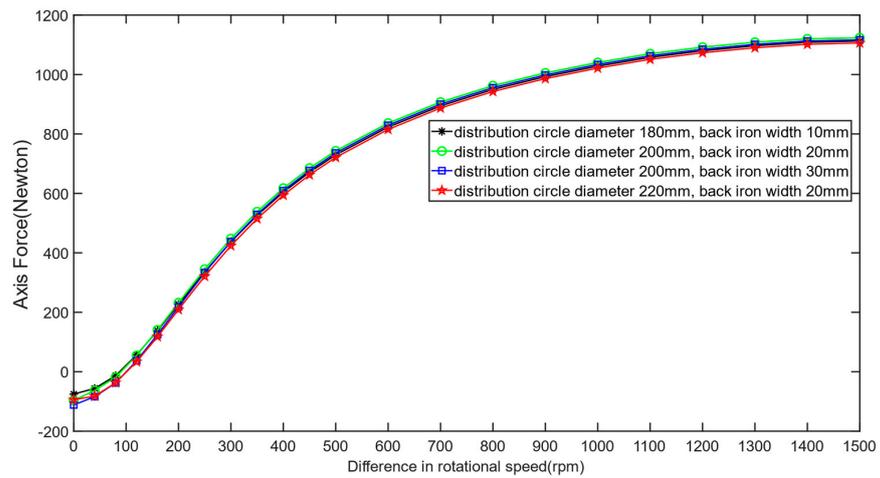
Figure 25. Conductor disc backplane distribution circle diameter and width−axial force curve.
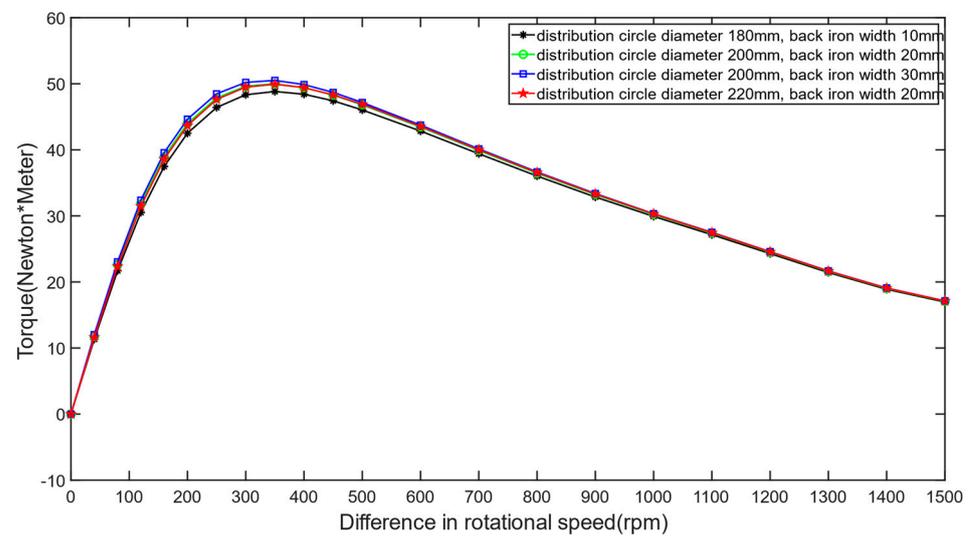
Figure 26. Conductor disc backplane distribution circle diameter and width—torque curve.
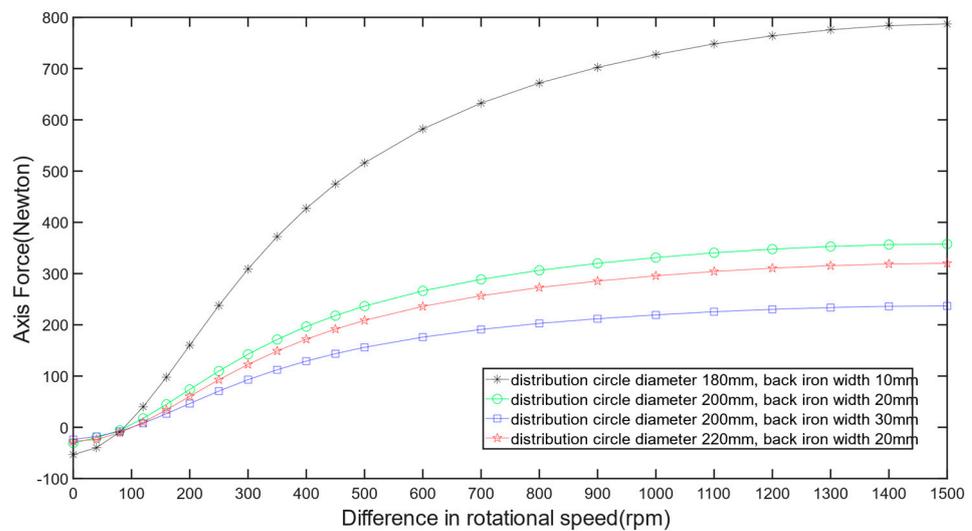
Figure 27. Difference in rotational speed—axial force curves per unit area of the conductor disc backplane.

5. Experiments and Results

The unique structure of the switching seal makes it difficult to measure the torque and axial force characteristics of the permanent magnet eddy current drive structure inside it. Currently, the only way to indirectly reflect the validity of the permanent magnet eddy current drive structure characteristics is by measuring the sealing of the switches. This is done by checking the flow rate at the spraying and water supply outlets. It should be noted, however, that such results only confirm the validity of the design concept of the PM eddy current drive structure, but they do not reflect the accuracy of the modeling of the transmission characteristics in question.

5.1. Test Prototypes and Test Methods

The test system was designed as shown in Figure 28, and its component equipment and key parameters are shown in Table 4. The test principle was to control the speed of the gear motor through the frequency converter and manually control the pressure and flow of the water supply system. In the left seal and the right seal at the outlet pipe, we set up a vibration-resistant pressure gauge, pressure sensors, and flow sensors, and used an adjustable DC power supply to power the sensors; the collected data were routed through the USB-6008 DAC to the host computer.

Figure 28. Test system and components.

Table 4. Device model and performance parameters.

Instrument Composition	Model	Parameters
Geared motors	YB3-380V-40-axis 3 kW	Speed RPM1480 Ratio 20
DAC	USB-6008	12-Bit,10 kS/s
Flow sensors	FLYW110	0.8~8 m^3/h,1.5%F.S.
Pressure sensors	CYB-20SA	0~6.3 Mpa, 0.25%F.S.
Converter	G120	3AC380V
Upper computer	Region R9000P	3.2 GHz
Shockproof pressure gauge	YN63-I	0~6.3 Mpa

The test methods were as follows: Firstly, install the prototype, use water to make sure all parts are wet, and check whether there is any leakage and whether the data acquisition system works normally. After, gradually increase the speed from 0 rpm to 50 rpm in 1 rpm increments, and collect the flow rate data for fifteen minutes at each speed, and take the average value of the time as the flow at that speed. Finally, gradually decrease the speed from 50 rpm to 0 rpm in 1 rpm increments, collect the flow data at each speed for fifteen minutes, and take the average value of the period as the flow at that speed.

5.2. Test Results

In Figure 29, the speed–flow diagrams of the two seal outlets are shown when the speed increases from 0 to 50 rpm and then decreases from 50 rpm to 0 rpm. It can be seen that, during the rotation speed-up phase, the switching seal changes from the cylinder condition to the internal spray condition at about 5 rpm, while during the rotation slow-down phase, the switching seal changes from the internal spray condition to the cylinder condition at about 10 rpm. The reason for this difference in speed between opening and switching is the influence of the working air gap. The permanent magnet eddy current structure of the switching seals has a working air gap of 2 mm when the left seal is closed, at which time the axial force and torque are larger (see Figures 15, 17 and 18), whereas when the right seal is closed the working air gap is 4 mm, and at this time the axial force and torque are smaller compared to the left seal closure condition (see Figures 16–18). This difference in speed between the switching conditions also verifies the correct analysis of the transmission characteristics of the permanent magnet eddy current structure.
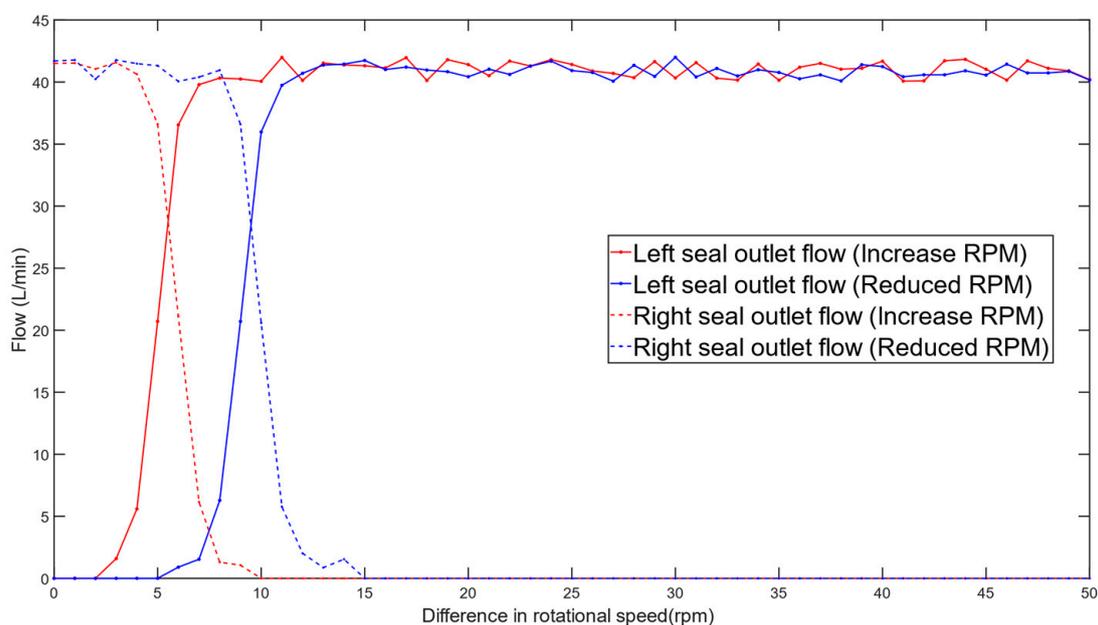
Figure 29. Flow diagram of seal outlets at different rotation speeds.

6. Conclusions

1. This study utilized the method of separation of variables to solve the electromagnetic field of the permanent magnet eddy current structure with a gap between the conductor disc and the backplane, and we derived the calculation methods for torque and axial force. Validation against results obtained using finite element methods showed that the analytical results were accurate, particularly under low-slip conditions, thus making this method suitable for electromagnetic field design calculations for such low-slip disc-type structures.

2. The working air gap of the permanent magnet eddy current structure plays a dominant role in the transmitted torque and axial force. Both torque and axial force decrease with increasing working air gap. The backplane air gap significantly influences the transmission characteristics of the switch-type seal in the low-slip region, leading to decreased torque transmission and initial axial force with increasing backplane air gap. However, in the high-slip region, the backplane air gap has little effect on the transmission characteristics.

3. The transmission characteristics of the permanent magnet eddy current structure show no significant relationship with the thickness of the conductor disc's backplane. However, under low-slip conditions, axial force and torque are related to the area of

the conductor disc's backplane facing the permanent magnet, with larger facing areas resulting in greater transmitted axial force and torque.

7. Patents

We have applied for a patent on the relevant technology, patent number CN202211533290.7, which is currently in the stage of substantive examination.

Data Availability Statement: Restrictions apply for the availability of these data. Data are available with the permission of the author.

Conflicts of Interest: Authors Teng Wang, Tao Song and Wenxiao Guo were employed by the company CCTEG Taiyuan Research Institute Co., Ltd. and Shanxi Tiandi Coal Mining Machinery Co., Ltd. The remaining authors declare that the research was conducted in the absence of any commercial or financial relationships that could be construed as a potential conflict of interest.

Appendix A. Derivation of the Governing Equations for Electromagnetic Fields

According to the fundamental equations of the magnetic field,

$$B = \mu_0 \mu_r H + \mu_0 M \tag{A1}$$

In a field with curl, there is

$$\nabla \times \mathbf{B} = \mu_0(\mu_r \nabla \times \mathbf{H} + \nabla \times \mathbf{M}) \tag{A2}$$

By introducing vector magnetic potential, Equation (A2) can be simplified to

$$\nabla \times (\nabla \times \mathbf{A}) = \mu_0(\mu_r \nabla \times \mathbf{H} + \nabla \times \mathbf{M}) \tag{A3}$$

By the curl calculation formula, there are

$$\nabla \times (\nabla \times \mathbf{A}) = \nabla(\nabla \cdot \mathbf{A}) - \nabla^2 \mathbf{A} \tag{A4}$$

According to the Coulomb gauge $\nabla \cdot \mathbf{A} = 0$, Equation (A4) can be reduced to Equation (A5). Tt is the electromagnetic field control equation for the layer model.

$$\nabla^2 \mathbf{A} = -\mu_0(\mu_r \nabla \times \mathbf{H} + \nabla \times \mathbf{M}) \tag{A5}$$

where $\mathbf{A}_k$ represents the magnetic vector of Layer k. μ_0 represents the vacuum permeability, with a value of $4\pi \times 10^{-7}$ H/m. μ_k represents the relative magnetic permeability of Layer k. $\mathbf{H}_k$ represents the magnetic field intensity of Layer k. $\mathbf{M}_k$ represents the magnetization intensity of Layer k.

Appendix B. Solving the Governing Equations of Electromagnetic Fields Using the Method of Separated Variables

Since only the eddy current components in the z-direction are considered, and the eddy current components in the z-direction are only related to x and y, we can neglect the magnetic field strength and the magnetic induction strength in the z-direction.

The solution to Laplace's equation in the separated variables method is given by

$$\nabla^2 \mathbf{A}_k = \frac{\partial^2 \mathbf{A}_k}{\partial x^2} + \frac{\partial^2 \mathbf{A}_k}{\partial y^2} = 0 \tag{A6}$$

Suppose that the solution of a second-order partial differential equation can be expressed as the product of functions of individual independent variables:

$$\mathbf{A}_k(x, y) = f(x)g(y) \tag{A7}$$

Substituting the above form of the solution into the given second-order Laplace equation,

$$\frac{f''(x)}{f(x)} + \frac{g''(y)}{g(y)} = 0 \tag{A8}$$

The transformation into two ordinary differential equations is achieved by setting both sides proportional to the derivative of some variable:

$$\begin{cases} \frac{f''(x)}{f(x)} = \lambda^2 \\ \frac{g''(x)}{g(x)} = -\lambda^2 \end{cases} \tag{A9}$$

Solving the two Equations (A10) and (A11) usually yields an eigenvalue problem on λ:

$$f''(x) = -\lambda f(x) \tag{A10}$$

$$g''(y) = \lambda g(y) \tag{A11}$$

Since the magnetic field exhibits a periodic distribution in the x-direction, $f(x)$ can be expressed as a Fourier series in complex form:

$$f(x) = \sum B_r e^{imx} \tag{A12}$$

The magnetic vector can be expressed by the separated variables method as follows:

$$\mathbf{A}_k(x, y) = \mathbf{A}_k(x) \cdot \mathbf{A}_k(y) \tag{A13}$$

Since the magnetic field exhibits a periodic distribution in the x-direction, the solution of the magnetic vector can be expressed as follows:

$$\mathbf{A}_k(x, y) = \sum_{j=\pm 1,3,5\cdots} \mathbf{A}_k(y) e^{imx} \tag{A14}$$

By introducing Equation (A14) into the electromagnetic field governing Equations (8), (10)–(12), (15), and (16), The general solution is shown in Equation (17) Considering the boundary conditions obtains the following matrix equation:

$$
\begin{bmatrix}
e^{m\cdot 0} & e^{-m\cdot 0} & 0 & 0 & 0 & 0 & 0 & 0 & 0 & 0 & 0 & 0 \\
e^{ma} & e^{-ma} & -e^{ma} & -e^{-ma} & 0 & 0 & 0 & 0 & 0 & 0 & 0 & 0 \\
0 & 0 & e^{mb} & e^{-mb} & -e^{mb} & -e^{-mb} & 0 & 0 & 0 & 0 & 0 & 0 \\
0 & 0 & 0 & e^{mc} & e^{-mc} & -e^{mc} & -e^{-mc} & 0 & 0 & 0 & 0 & 0 \\
0 & 0 & 0 & 0 & e^{\lambda_1 d} & e^{-\lambda_1 d} & -e^{\lambda_1 d} & -e^{-\lambda_1 d} & 0 & 0 & 0 & 0 \\
0 & 0 & 0 & 0 & 0 & 0 & e^{me} & e^{-me} & -e^{me} & -e^{-me} & 0 & 0 \\
0 & 0 & 0 & 0 & 0 & 0 & 0 & 0 & 0 & 0 & e^{\lambda_2 f} & e^{-\lambda_2 f} \\
\frac{e^{ma}}{\mu_1} & -\frac{e^{-ma}}{\mu_1} & -\frac{e^{ma}}{\mu_2} & \frac{e^{-ma}}{\mu_2} & 0 & 0 & 0 & 0 & 0 & 0 & 0 & 0 \\
0 & 0 & \frac{e^{mb}}{\mu_2} & -\frac{e^{-mb}}{\mu_2} & -\frac{e^{mb}}{\mu_3} & \frac{e^{-mb}}{\mu_3} & 0 & 0 & 0 & 0 & 0 & 0 \\
0 & 0 & 0 & 0 & m\frac{e^{mc}}{\mu_3} & -m\frac{e^{-mc}}{\mu_3} & -\lambda_1\frac{e^{\lambda_1 c}}{\mu_4} & \lambda_1\frac{e^{-\lambda_1 c}}{\mu_4} & 0 & 0 & 0 & 0 \\
0 & 0 & 0 & 0 & 0 & 0 & \lambda_1\frac{e^{\lambda_1 d}}{\mu_4} & -\lambda_1\frac{e^{-\lambda_1 d}}{\mu_4} & -m\frac{e^{md}}{\mu_5} & m\frac{e^{-md}}{\mu_5} & 0 & 0 \\
0 & 0 & 0 & 0 & 0 & 0 & 0 & 0 & m\frac{e^{me}}{\mu_5} & -m\frac{e^{-me}}{\mu_5} & -\lambda_2\frac{e^{\lambda_2 e}}{\mu_6} & \lambda_2\frac{e^{-\lambda_2 e}}{\mu_6}
\end{bmatrix}
\begin{bmatrix} C_1 \\ D_1 \\ C_2 \\ D_2 \\ C_3 \\ D_3 \\ C_4 \\ D_4 \\ C_5 \\ D_5 \\ C_6 \\ D_6 \end{bmatrix}
=
\begin{bmatrix} 0 \\ \frac{iB_r}{m} \\ -\frac{iB_r}{m} \\ 0 \\ 0 \\ 0 \\ 0 \\ 0 \\ 0 \\ 0 \\ 0 \\ 0 \end{bmatrix}
\tag{A15}
$$

Appendix C. Detailed Boundary Conditions

$$
\begin{cases}
\dfrac{\partial \mathbf{A}_{1n}}{\partial x} = \dfrac{\partial \mathbf{A}_{2n}}{\partial x}\bigg|_{y=a} \\[2mm]
\dfrac{1}{\mu_1}\dfrac{\partial \mathbf{A}_{1n}}{\partial y} = \dfrac{1}{\mu_2}\dfrac{\partial \mathbf{A}_{2n}}{\partial y}\bigg|_{y=a}
\end{cases}
\tag{A16}
$$

$$
\begin{cases}
\dfrac{\partial \mathbf{A}_{2n}}{\partial x} = \dfrac{\partial \mathbf{A}_{3n}}{\partial x}\bigg|_{y=b} \\[2mm]
\dfrac{1}{\mu_2}\dfrac{\partial \mathbf{A}_{2n}}{\partial y} = \dfrac{1}{\mu_3}\dfrac{\partial \mathbf{A}_{3n}}{\partial y}\bigg|_{y=b}
\end{cases}
\tag{A17}
$$

$$
\begin{cases}
\dfrac{\partial \mathbf{A}_{3n}}{\partial x} = \dfrac{\partial \mathbf{A}_{4n}}{\partial x}\bigg|_{y=c} \\[2mm]
\dfrac{1}{\mu_3}\dfrac{\partial \mathbf{A}_{3n}}{\partial y} = \dfrac{1}{\mu_4}\dfrac{\partial \mathbf{A}_{4n}}{\partial y}\bigg|_{y=c}
\end{cases}
\tag{A18}
$$

$$
\begin{cases}
\dfrac{\partial \mathbf{A}_{4n}}{\partial x} = \dfrac{\partial \mathbf{A}_{5n}}{\partial x}\bigg|_{y=d} \\[2mm]
\dfrac{1}{\mu_4}\dfrac{\partial \mathbf{A}_{4n}}{\partial y} = \dfrac{1}{\mu_5}\dfrac{\partial \mathbf{A}_{5n}}{\partial y}\bigg|_{y=d}
\end{cases}
\tag{A19}
$$

$$
\begin{cases}
\dfrac{\partial \mathbf{A}_{5n}}{\partial x} = \dfrac{\partial \mathbf{A}_{6n}}{\partial x}\bigg|_{y=e} \\[2mm]
\dfrac{1}{\mu_5}\dfrac{\partial \mathbf{A}_{5n}}{\partial y} = \dfrac{1}{\mu_6}\dfrac{\partial \mathbf{A}_{6n}}{\partial y}\bigg|_{y=e}
\end{cases}
\tag{A20}
$$

where a, b, c, d, e, and f are the y coordinates of each layer interface in the layer model, as shown in Figure 5, whose values are determined by the parameters of the permanent magnet eddy current structure.

References

1. Li, F. Research Status on Internal Spraying Technology of Gateway Driving Equipment. *Coal Sci. Technol.* **2017**, *45*, 89–92. [CrossRef]
2. Cheng, D. *Machinery Design Manual*, 6th ed.; Chemical Industry Press: Beijing, China, 2016; Volume 3, pp. 276–301.
3. Yang, C. Transmission Characteristics of Axial Asynchronous Permanent Magnet Couplings. *J. Mech. Eng.* **2014**, *50*, 76–84. [CrossRef]
4. Dai, X.; Liang, Q.; Cao, J.; Long, Y.; Mo, J.; Wang, S. Analytical Modeling of Axial-Flux Permanent Magnet Eddy Current Couplings with a Slotted Conductor Topology. *IEEE Trans. Magn.* **2016**, *52*, 8000315. [CrossRef]
5. Yang, C.; Zhu, L.; Wu, Y. Speed Regulation Characteristics of Slotted Disc-Type Asynchronous Magnetic Coupler. *Electr. Mach. Control. J.* **2021**, *25*, 130–138. [CrossRef]
6. Xu, Z.; Wu, R.; Xiao, M. Torque and speed performance study of disk type synchronous magnetic coupler. *Sci. Bull. Mech. Eng.* **2022**, *84*, 211–222.
7. Boules, N. Prediction of No-Load Flux Density Distribution in Permanent Magnet Machines. *IEEE Trans. Ind. Appl.* **1985**, *A-21*, 633–643. [CrossRef]
8. Shi, T. Analytical Modeling, Analyzing and Optimal Designing of Permanent Magnet Eddy-Current Couplings. Ph.D. Thesis, Northeastern University, Boston, MA, USA, 2018.
9. Zhang, Z.; Han, Q.; Xu, X.; Yan, Y.; Peng, C. Air Gap Magnetic Field Calculation of Permanent Magnet Direct Drive Generator Based on Conformal Mapping and Magnetic Equivalent Circuit Method. *Trans. China Electrotech. Soc.* **2023**, *38*, 703–710.
10. Smith, A.C.; Willsamson, H.; Benhama, N.; Counter, L.F. Magnetic Drive Couplings. In Proceedings of the International Electric Machines and Drives Conference, Canterbury, UK, 13 September 1999.

11. Wang, J.; Lin, H.; Fang, S.; Huang, Y. A General Analytical Model of Permanent Magnet Eddy Current Couplings. *IEEE Trans. Magn.* **2014**, *50*, 8000109. [CrossRef]
12. Razavi, H.K.; Lamperth, M.U. Eddy-Current Coupling with Slotted Conductor Disk. *IEEE Trans. Magn.* **2006**, *42*, 405–410. [CrossRef]
13. Dai, X.; Liang, Q.; Ren, C.; Cao, J.; Mo, J.; Wang, S. Analytical Solution of Magnetic Field in Permanent-Magnet Eddy-Current Couplings by Considering the Effects of Slots and Iron-Core Protrusions. *J. Magn.* **2015**, *20*, 273–283. [CrossRef]
14. Yang, F.; Liu, L. Magnetic Field Analysis of Permanent Magnet Magnetic Coupler Based on Ansoft Maxwell. In Proceedings of the Application of Artificial Intelligence and Modern Information Technology in the Coal Industry 2019 Annual Conference; China Coal Society Mine Mechatronics Professional Committee: Enshi, China, 2019; pp. 88–90.
15. *Wolfgang Nolting Electrodynamics*; Springer: Cham, Switzerland, 2016; ISBN 9783319401676.
16. Arfken, G.B.; Weber, H.J.; Harris, F.E. *Mathematical Methods for Physicists a Comprehensive Guide*; Elsevier: Amsterdam, The Netherlands, 2013; ISBN 9780123846549.
17. Conway, J. *Functions of One Complex Variable*; Springer Nature: Berlin/Heidelberg, Germany, 1973.
18. Russell, R.; Norsworthy, K.J. Eddy Currents and Wall Losses in Screened-Rotor Induction Motors. *Proc. IEE-Part A Power Eng.* **1958**, *105*, 163–175. [CrossRef]
19. Wang, M.; Kou, B.; Zhang, L.; Xu, J. Characteristics Analysis for Axial-Flux Permanent Magnet Eddy Current Brake with Slotted Disc. Available online: https://ieeexplore.ieee.org/document/9845986 (accessed on 11 August 2022).